FED-Vol. 157, Unsteady Flows – 1993
ASME 1993

NUMERICAL STUDIES OF NON-NEWTONIAN PULSED FLOW IN A FEMORAL BRANCHED VESSEL

Rupak K. Banerjee and Young I. Cho
Department of Mechanical Engineering and Mechanics
Drexel University
Philadelphia, Pennsylvania

Lloyd H. Back
Jet Propulsion Laboratory
California Institute of Technology
Pasadena, California

ABSTRACT

A numerical investigation was carried out to acquire an understanding of local flow phenomena in an arterial branch model similar to the femoral artery of man with a branch angle of 90 degree. Flow separations were not only found along the main lumen wall opposite to the branch during the early decelerating phase of the systolic part of the pulse cycle, and also at the proximal wall of the branch. Due to the tri-phasic nature of the femoral pulse, milder recirculating flows were observed at the wall of the main lumen located near the branch. Recirculating zones were functions of both temporal and spatial parameters. The distal wall of the branch and the wall of the main lumen near the branch orifice showed elevated shear rate and shear stress values. During a cardiac cycle, enhanced fluctuation of shear rate and shear stress from positive to negative values were observed near the branch region. The changes in hydrodynamic flow parameters near branches may be associated with site-specific lesion formation regions that have been observed.

NOMENCLATURE

d = lumen width
n_j = normal vector
p = pressure
p_1 = wall pressure at reference location (initial node)
p_i = wall pressure at any downstream nodes
s_i = stress vector
t = time
T = period of heart beat
u_i = velocity vector
x = distance along the main lumen
y = distance along the branch lumen
α = dimensionless frequency parameter, or Womersley number
$\dot{\gamma}$ = shear rate
ϵ = penalty parameter
η = viscosity
ν = kinematic viscosity ($= \eta/\rho$)
ρ = density
τ = shear stress
ω = circular frequency, $2\pi/T$
τ_w = wall shear stress

subscripts
s = main lumen
b = branch lumen
$*$ = numerically computed valued

INTRODUCTION

The human circulatory system consists of many anatomically different arterial branches (Fig. 1A), with various branch angles, diameter ratios of the branch to the main lumen, downstream to upstream main lumen diameter ratios; and main lumen and branch curvatures. As seen in Fig. 1B, lesions often occur at these branch sites (Nerem and Levesque [1987]) and subsequently, the fluid dynamics of arterial flow and the related mass transport have been implicated to be factors in the genesis of atherosclerotic lesions (Fry [1973]). Consequently, there is much work needed to sort out the various geometrical and hydrodynamic variables that govern the fluid dynamic behavior in branch flow.

Non-Newtonian fluid characteristics of blood in branch flow with pulsatility create difficulties in carrying out a quantitative analysis. Flow impingement which occurs at a branch junction often produces a thinning of the shear layer in the main vessel and branch downstream of the impingement location, resulting in a local increase in the shear stress. Flow separation is often observed in the branch site, but the conditions for which separation occurs are not well documented [Lutz et al. 1983]. Liepsch et al. [1982] measured and calculated flow parameters of a laminar flow in a 90° bifurcation. Increase in Reynolds number and branch flow ratio caused an increase in the size of the recirculation zone in the main lumen wall opposite to the branch. Moravec and Liepsch [1983] experimentally investigated effects of Newtonian and non-Newtonian fluids for a steady flow in a 3-D doubly branched renal artery and found differences in flow profile distal to the bifurcations.

The motivation for this investigation was based on an earlier clinical trial studying the effects of lipid lowering on human atherosclerosis. Detailed statistics were reported by Cho et al. [1985]. Angiograms from 147 patients clearly indicated strong hydrodynamic effects on the development of atherosclerosis in femoral arterial vessels. Branch related lesions were classified as i) plaques along the opposite wall to the branch and ii) proximal and distal constrictions of the branch itself. In addition, the discrete lesions appeared to be located along the inner curvature of the branch

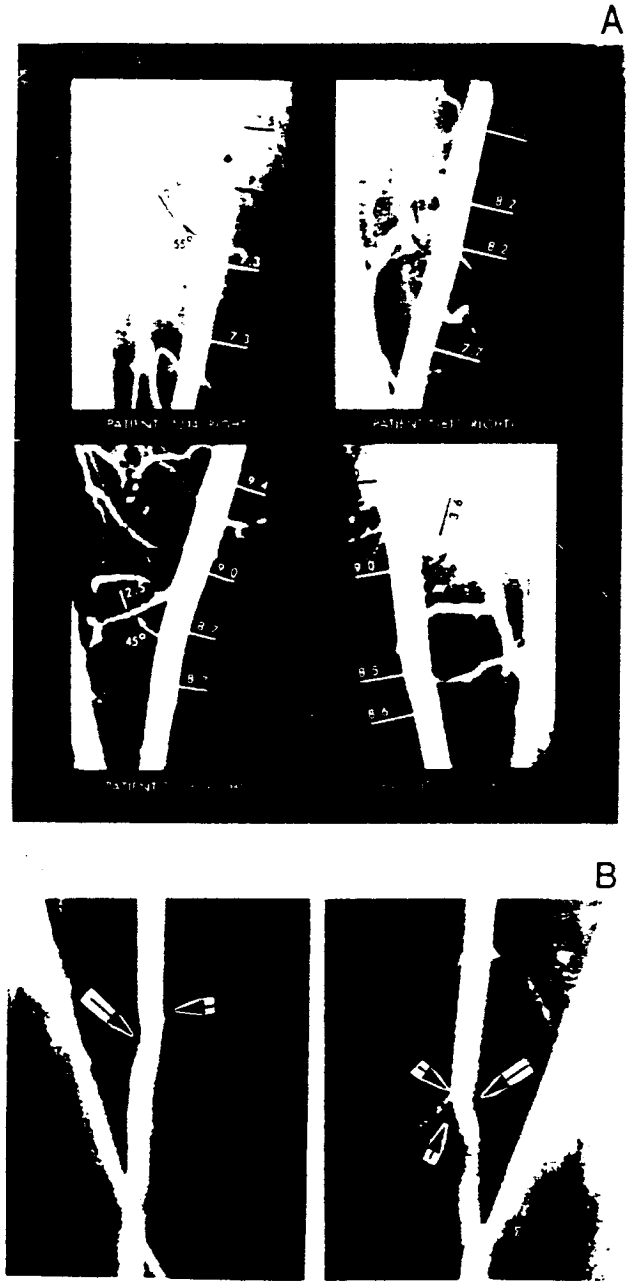

Fig. 1 Segments of femoral artery angiogram of man is shown in fig. 1A. Vessel sizes are in mm. The striking symmetric locations of apparent lesions opposite branches are demonstrated in fig. 1B. Blood flow is from top to bottom.

sites, and hardly any lesions were found along the outer curvature. Earlier experimental studies by Back et al. [1986] and Cho et al. [1985] isolated effects of branch flow rate, branch angle, and the Reynolds number on pressure and flow fields in arterial branch models. However, these studies were limited to the region opposite to the branch only. The overall flow field and flow separation in the branch itself were not reported.

Perktold [1989] conducted non-Newtonian blood (Casson model) flow calculations and in an arterial bifurcation. Velocity, wall shear stress, and non-Newtonian viscosity results were presented for a bi-phasic flow (a forward flow followed by a reverse flow) for a main lumen diameter of 4 cm and diameter ratio of 0.5. However, Perktold's study can not be related to physiological flow in the femoral artery of humans because the instantaneous flow considered was not tri-phasic (a forward flow, then a reverse flow followed by a forward flow) in nature and the diameter was smaller compared to the adult femoral arterial size of 6 to 7 mm. Khodadadi [1992] reported wall pressure and shear stress variation, along with the dynamic recirculation zone, in a 90° branch geometry having rectangular cross-section which however, is physiologically unrealistic.

The objective of the present study was to numerically calculate temporal and spatial dependent fluid parameters, including velocity profile, shear rate, shear stress and pressure drop in a branch junction arterial model in order to understand the flow field at the site-specific lesion formation regions.

METHODS

The present investigation is based on a femoral artery angiogram (Fig. 1). The focus of this study is on a branch angle of 90°, which is commonly observed in the downstream portion of the femoral artery. The ratio of branch to main lumen width d_b/d_s is 0.4. The arterial branch model has upstream and downstream main lumen widths of 0.631 cm and branch width of 0.252 cm which is somewhat similar to femoral artery branches of man reported earlier by Cho et al [1985].

This study deals with the time-dependent solution of an incompressible, non-Newtonian fluid for the selected geometry. The flow is taken to be confined by rigid walls. Though this study is limited and does not explore complete 3-D flow phenomenon, the flow simulation for the 2-D flow presents further insight into the branch flow characteristics. As compared to a 2-D pulsed flow simulation, a 3-D pulsed flow requires large CPU time and memory which are beyond the scope of the present computation facility.

The flow is described by the conservation equations of fluid mass and momentum. A finite element method (FEM) is used to solve the following two conservation equations to obtain the velocity, pressure, and wall shear stress distributions;

$$u_{i,i} = 0 \tag{1}$$

$$\rho\left[\frac{\partial u_i}{\partial t} + u_j u_{i,j}\right] = \sigma_{ij,j} + \rho f_i \tag{2}$$

where i, j = 1, 2 for 2-D flow. u_i is the ith component of the velocity vector, ρ is density, σ_{ij} is stress tensor, and f_i is the body force. Further,

$$\sigma_{ij} = -p\,\delta_{ij} + \tau_{ij} \tag{3}$$

where

$$\tau_{ij} = 2\,\eta_{ij}\,\varepsilon_{ij} \tag{4}$$

$$\varepsilon_{ij} = 0.5\,(u_{i,j} + u_{j,i}) \tag{5}$$

Here, p is the pressure, τ_{ij} is the deviatoric stress tensor, ε_{ij} is the shear rate tensor, η_{ij} is the tensor viscosity, and δ_{ij} is the Kronecker delta. Axial components of flow along the main lumen are reported along the x and y directions where y direction is parallel to the branch axis.

The stress vector s_i at a point on the boundary of a fluid element is defined by

$$s_i = \sigma_{ij}\,n_j \tag{6}$$

For a known element and the solution field, the stress component s_i on the boundary at the Gaussian integration points is evaluated. Subsequently, the normal and tangential components of stress vectors are obtained after applying appropriate transformations.

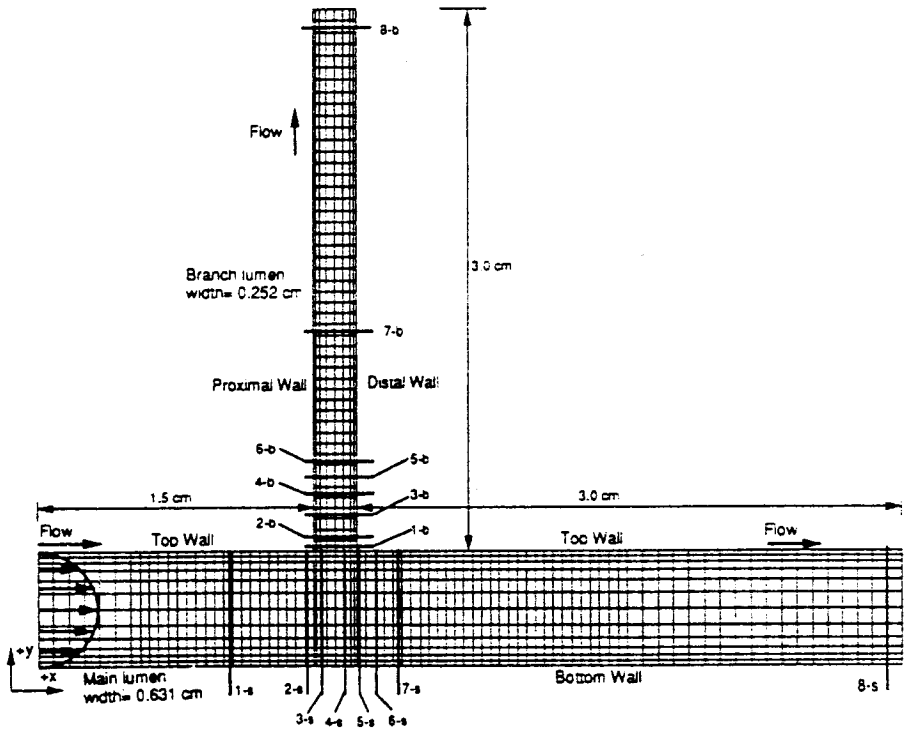

Fig. 2 The mesh plot along with dimension of a 90° branch femoral artery. Also shown are the various axial locations (1-s to 8-s for main lumen and 1-b to 8-b for branch lumen) for which flow data are reported.

The Galerkin formulation (Baker [1983]) using nine nodal quadrilateral elements is applied herein to discretize the above continuity and momentum equations, which result in a set of nonlinear algebraic equations of the form

$$M\frac{du}{dt} + K(u)\,u = F \qquad (7)$$

where K(u) is the global system matrix developed from the momentum balance, M is the mass matrix, u is the velocity unknown, and F is the forcing function (including body forces and boundary conditions).

The mesh plot for the artery is shown in Fig. 2. Spatial variations of velocity across the flow, at various time steps, are obtained at axial locations marked by 1-s to 8-s for main lumen and 1-b to 8-b for branch lumen. Time histories of shear rate and pressure drop are reported for both wall elements located at axial locations of 1-s to 8-s for main lumen and 1-b to 8-b for branch lumen. Shear stress at various time steps is calculated along the arterial walls of both main and branched lumens.

Often the FEM is not directly applied to the system of equations but rather to a perturbed system of equations in which the continuity requirement is weakened by

$$u_{i,i} = -\varepsilon p \qquad \text{where } \varepsilon = 1 \times 10^{-9} \qquad (8)$$

For high aspect ratios of the elements, a small penalty parameter is recommended (Banerjee et al. [1992]). Physically, this can be equated to simulating the flow having an insignificant compressibility effect. This approach has the advantage of temporarily eliminating one of the dependent variables, p^*, which is later recovered by post-:ssing from the velocity field by

$$p^* = -u_i^*{}_{,i}/\varepsilon \qquad (9)$$

Clearly, both the pressure and velocity fields are determined in the calculation method, as must be the case.

The normalized instantaneous tri-phasic inlet velocity profile (u/u_{peak}), Fig. 3, has been replotted from the *in-vivo* velocity profile measurement (Risoe and Wille [1978]) in the core region. The peak input velocity (u_{peak}) is 36.3 cm/sec at t= 0.122 s. Risoe and Wille used an ultrasound Doppler flow meter to obtain the instantaneous velocity measurements. In the present study, the normalized tri-phasic inlet velocity profile is used as an instantaneous input for the numerical calculations. Considering the relatively long entry length of the femoral artery, for different time steps of the pulse cycle, fully developed flows are used as spatial distribution for inlet flows (Schultz [1972] and Dewey [1978]). The selected time steps for flow analysis have been marked from No. 1 to No. 8 in Fig. 3. The no-slip boundary condition has been specified on the rigid arterial wall. At the outlet no boundary condition is specified.

The matrix equation (7), representing a discrete analog of the original equations for an individual fluid element, is constructed, assembled, and solved. For spatial integration, the number of iteration steps is limited to ten at each time step with a combination of the successive substitution method and quasi-Newton scheme. The numerical simulation of a pulsatile flow requires a time integration method. The implicit time integration scheme used in the current study is the second order trapezoidal method with a variable time step, which depends on the magnitude of temporal input velocity and its gradient change. Depending on temporal variation of velocity the time steps varied between 1×10^{-3} to 1×10^{-5} s. The finite-element computer code FIDAP [1991] is used to formulate and solve this matrix equation. The IBM-3090 is used with TEMPLATE graphics for post-processing, and the results are down-loaded to an Apple-Macintosh II computer.

In comparison to the core elements of the lumen the element sizes near the wall are kept smaller to achieve a better accuracy of flow parameters. The aspect ratio of nine-nodal quadrilateral elements is chosen to be less than 10. For validation of the numerical

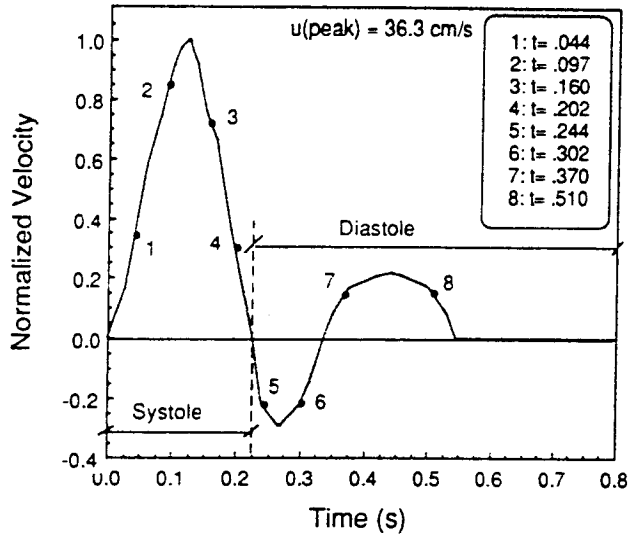

Fig. 3 Normalized form of the *in-vivo* velocity pulse near the core of the femoral artery along a pulse cycle obtained by doppler flow meter. Also shown are the various time steps (No. 1 to No. 8) for which flow data are reported.

computation, two separate computer modeling runs at peak systolic flow with different convergence criteria have been performed which are as follows: both the relative velocity error with respect to a previous step and relative residue error as compared to the initial value are set to be 2% and 1% respectively (Banerjee et al. [1992]). Furthermore, the overall convergence is confirmed by increasing the total number of meshes by 20% from that of the previous run, and the two results are compared to check for accuracy. When the improvement with 20% more meshes is less than 1% in velocity vectors, wall shear stress, and pressure, the computation is considered accurate. The analysis of results is from the computation with the least CPU time, i.e., less than 2% for both relative velocity and relative residue errors.

In the present investigation, the Carreau model is used to represent the blood viscosity whose model constants are obtained by curve-fitting of available shear-rate dependent blood viscosity data in the literature (Cho and Kensey [1991])

$$\eta = \eta_\infty + (\eta_0 - \eta_\infty)\left[1 + (\lambda\dot{\gamma})^2\right]^{\frac{n-1}{2}} \qquad (10)$$

where λ (characteristics time) = 3.313 s, n = 0.3568, η_0 = 0.56 poise, η_∞ = 0.0345 poise.

In order to calculate viscosity in the flow field locally, the local shear rate, $\dot{\gamma}$, is calculated from velocity gradient through the second

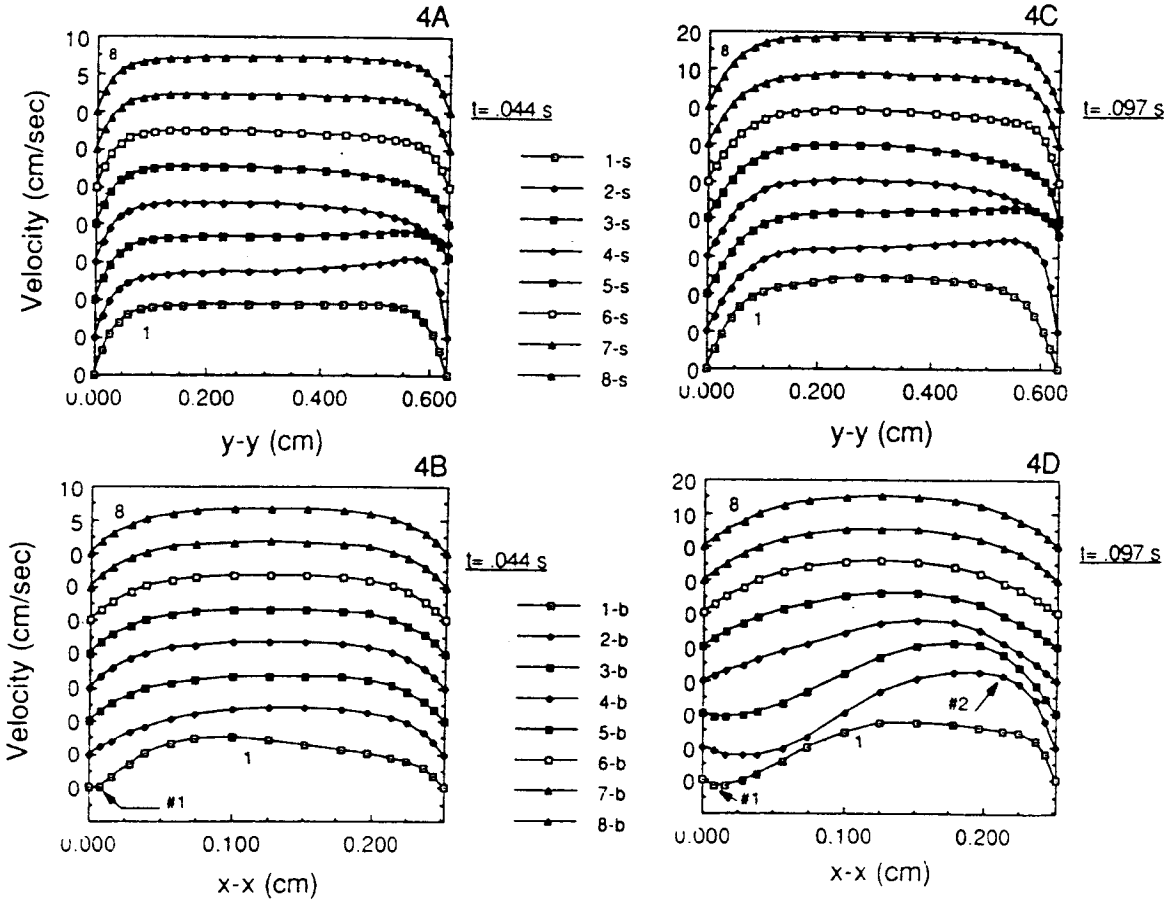

Fig. 4A-4D Velocity distributions across the main and branch lumen at different axial locations for various time steps of a pulse cycle.

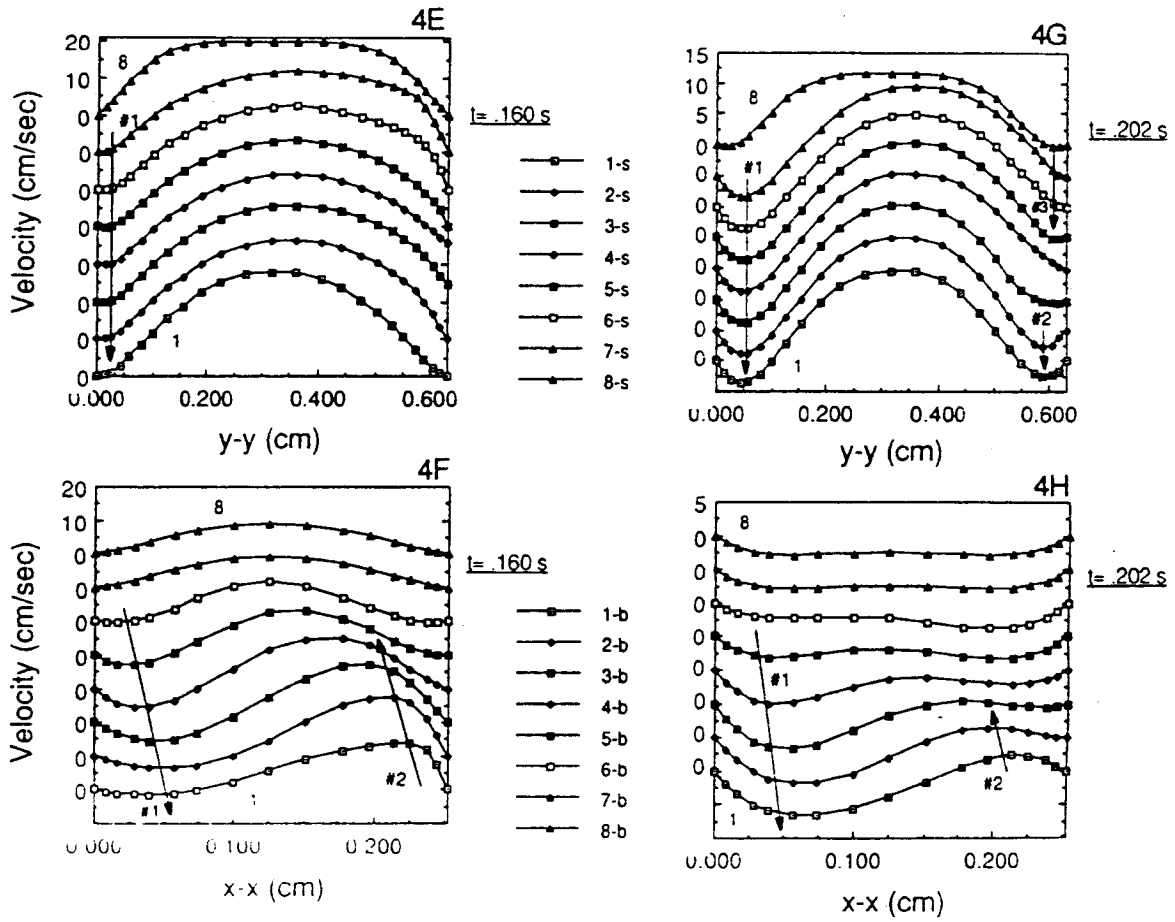

Fig. 4E-4H Velocity distributions across the main and branch lumen at different axial locations for various time steps of a pulse cycle.

invariant of the rate of strain tensor, $\Pi_{\dot{\gamma}}$, as follows:

$$\dot{\gamma} = \sqrt{\frac{1}{2}\Pi} = \sqrt{\frac{1}{2}\left[\sum_i \sum_j \dot{\gamma}_{ij}\,\dot{\gamma}_{ji}\right]} \qquad (11)$$

After the local viscosity is determined using Carreau model, Eq. (10), the local shear stress, τ (= $\eta\,\dot{\gamma}$), is calculated. Blood with a constant density of 1.05 g/cm^3 and infinite shear rate kinematic viscosity ν_∞ (=η_∞/ρ) are used in the calculations. The pulse rate is 75 bpm. Hence, the dimensionless frequency parameter [α = 0.5 d $(\omega/\nu)^{0.5}$] for the femoral artery of man is found to be 4.87.

RESULTS AND DISCUSSION

Figures 4A-4P show axial velocity profiles at different locations (Fig. 2) across the main and branched lumen for various time steps (Fig. 3). At t = 0.044 sec, Figs. 4A and 4B show velocity profiles at axial locations in the main lumen (1-s to 8-s) and the branched lumen (1-b to 8-b), respectively. Velocity plots at time t = 0.044 s (Figs. 4A and 4B) and 0.097 s (Figs. 4C and 4D) represent accelerating flow whereas those at time t = 0.160 s (Figs. 4E and 4F) and 0.202 s (Figs. 4G and 4H) represent decelerating flow during the latter part of systole. In contrast, velocity plots at time t = 0.244 s (Figs. 4I and 4J) represent accelerating negative or reverse flow whereas those at time t = 0.302 s (Figs. 4K and 4L) represent decelerating negative flow in early diastole. Similar to the systolic flow, velocity plots at time t = 0.370 s (Figs. 4M and 4N) represent accelerating flow whereas those at time t = 0.510 s (Figs. 4O and 4P) represent decelerating flow in mid-diastole. Negligible flow was reported during late diastole which is represented by the time period between t = 0.55 s and 0.80 s (Risoe and Wille [1978]). Due to the negligible flow for approximately 30% of the pulse cycle, the flow parameters for consecutive cycles are independent of each other.

For accelerating systolic flow the proximal branch wall shows increased negative or reverse flow (i.e., arrow #1 in Figs. 4B and 4D) from t = 0.044 s to t = 0.097 s where the axial velocity is -1.96 cm/s. Although the main lumen flow is of positive accelerating type, the negative flow near the proximal apex of the branch indicates the existence of an early recirculating region. In contrast, the distal branch wall shows a sharp velocity gradient and higher positive velocity of 17.5 cm/s for plot No. 2-b (i.e., arrow #2 in Fig. 4D). The axial velocity then decreases along the axial flow direction in the branch lumen. Near the apex of the distal branch the magnitude of velocity for plot No. 1-b, is much less than for plot No. 2-b (i.e., arrow #2 in Fig. 4D).

During the flow decelerating phase of systole the recirculation intensity, measured by the negative velocity, recirculation length, measured by the axial distance of negative velocity, and recirculation height, measured by the lateral extent of negative velocity, at the proximal branch wall increases from t = 0.160 s to t = 0.202 s (i.e., arrow #1 in Figs. 4F and 4H). For plot No. 1-b in Fig. 4F, the maximum negative velocity is -1.57 cm/s, whereas it is -6.53 cm/s for plot No. 1-b in Fig. 4H which indicates a higher intensity of recirculation. Similarly, for plot No. 1-b in Fig. 4F, the lateral extent of negative velocity is 0.078 cm from the proximal wall, whereas it is 0.17 cm for plot No. 1-b in Fig. 4H, which indicates a larger

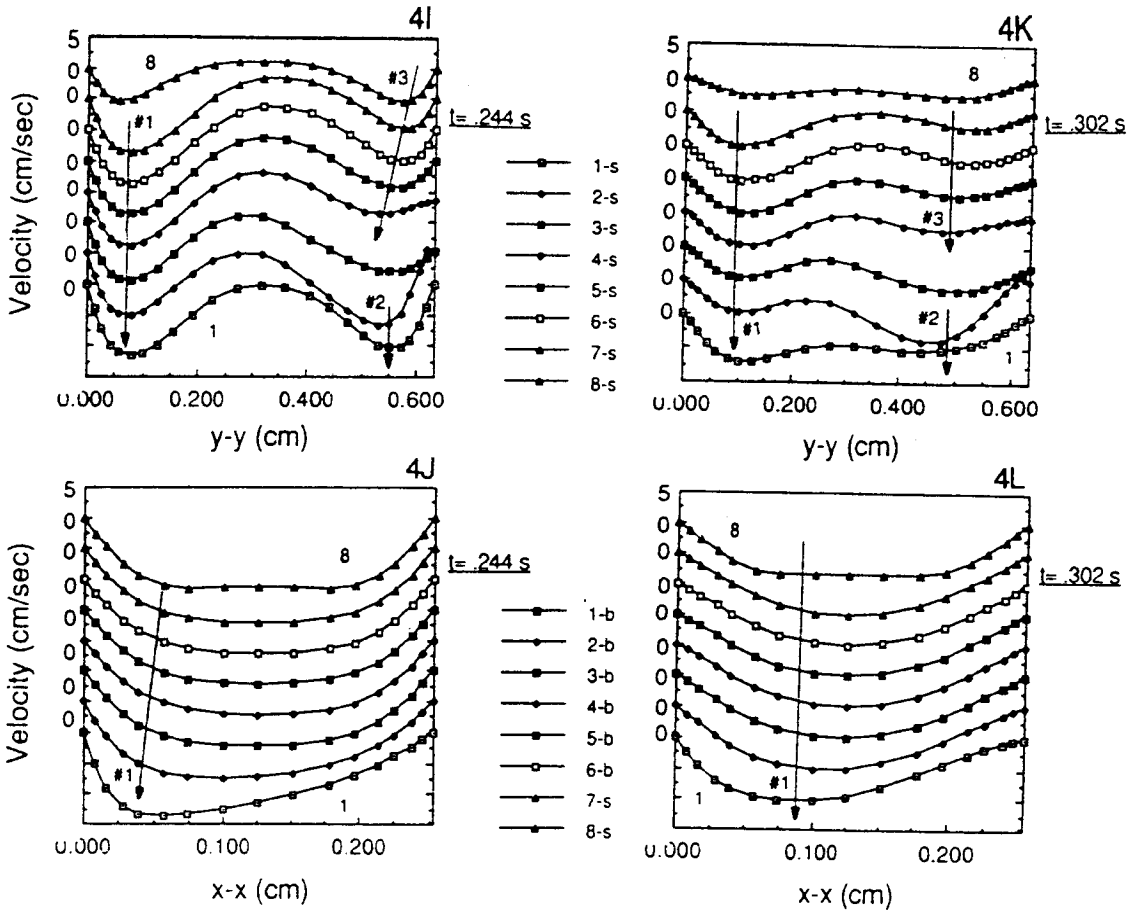

Fig. 4I-4L Velocity distributions across the main and branch lumen at different axial locations for various time steps of a pulse cycle.

recirculation thickness. Along the axial direction the extent of negative velocity is observed up to location No. 6-b in Fig. 4F, whereas it is prolonged further downstream in Fig. 4H, which indicates an increasing recirculation length. In addition, for the decelerating flow phase of systole, the distal wall experiences a reduction of high positive velocity along the wall (i.e., arrow #2 for plots No. 1-b to 5-b in Fig. 4F and 1-b to 3-b in Fig. 4H).

Generation of recirculating flow in the branch lumen is observed during systole. In addition, co-exsistence of high velocity at the distal branch wall and low velocity at the proximal branch wall is observed.

Interestingly, during the decelerating phase of systole, another recirculating region develops at the main lumen wall opposite to the branch. Formation of recirculating flow is observed at t = 0.160 s (i.e., arrow #1 for plots No. 7-s to 1-s in Fig. 4E) and subsequently, the intensity, length, and height of the recirculation region increase as the flow reaches late systolic period, at t = 0.202 s (i.e., arrow #1 for plots No. 7-s to 1-s in Fig. 4G). Further, at the top wall, near the branch apex, mild recirculations are observed in Fig. 4G (i.e., arrow #2 for plots No. 2-s to 1-s upstream of the proximal wall, and arrow #3 for plots No. 7-s to 5-s downstream of the distal wall.

The recirculating zones at the main lumen walls is further reinforced during negative diastolic flow (i.e., arrows #1, #2 and #3 in Figs. 4I and 4K). During early diastolic flow, Figs. 4J and 4L (i.e., arrow #1) show complete flow reversal in the branch region, indicating suction of fluid from the proximal branch wall into the main lumen. Velocity profiles in mid-diastole shown in Figs. 4M-4P re similar to the systolic flow, but velocities are lower in magnitude.

Figures 5A-5D show calculations of shear rate at the wall during the pulse cycle at different axial locations (Fig. 2). For wall locations 1-8 refer to Fig. 2. The main lumen opposite to the branch, denoted as bottom wall, shows high shear region at t = 0.092 s which represents high instantaneous velocity gradient ($\partial u/\partial t$) during systole. The high shear rate near the inlet section decreases from $\dot{\gamma}$ = 310 s^{-1}. (i.e., arrow #1 for plot No. 1 in Fig. 5A) to a reduced positive value of 216 s^{-1} at branch region (i.e., plot No. 5 in Fig. 5A). As discussed earlier, a prolonged recirculating region is observed at the bottom wall from t = 0.152 s (i.e., early systolic decelerating flow) to t = 0.32 s (i.e., mid-diastolic region). The maximum negative shear rate is -274 s^{-1} (i.e., arrow #2 plot No. 1 in Fig. 5A).

It is interesting to note that the top wall, near the branch apex, experiences a very high shear rate. Although the top wall in Fig. 5B shows a similar trend of shear rate as in Fig. 5A, the apex of the proximal branch wall (i.e., arrow #1 for plot No. 2 in Fig. 5B) and distal branch wall (i.e., arrow #2 for plot No. 5 in Fig. 5B) show elevated positive shear rates. For plot No. 2 in Fig. 5B, the shear rate increases three fold to a value of 907 s^{-1} at t = 0.104 s whereas for plot No. 5 the shear rate increases to a value of 711 s^{-1} at t = 0.117 s.

The proximal wall near the branch apex, Fig. 5C, experiences negative shear for a prolonged period of time, i.e., from t = 0.05 s to t = 0.34 s (i.e., arrow #1 for plot No. 1 in Fig. 5C). Maximum negative shear rate of -514 s^{-1} at t = 0.243 s (i.e., arrow #2 for plot No. 1 in Fig. 5C) is observed at this location. At farther downstream locations along the proximal wall of the branch, the intensity and duration of recirculating flow significantly reduce with time. During systole, downstream locations of the proximal branch wall experience the maximum value of shear rate at different times (i.e.,

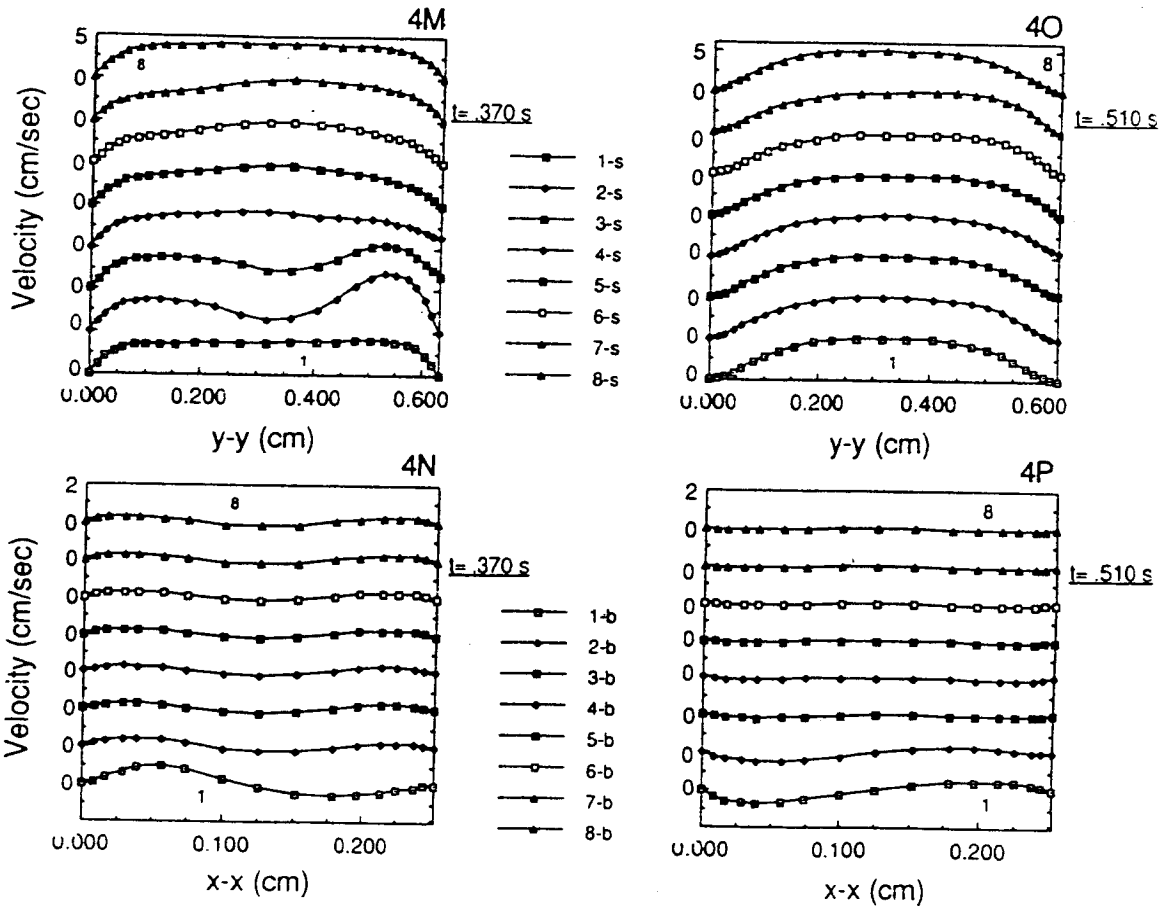

Fig. 4M-4P Velocity distributions across the main and branch lumen at different axial locations for various time steps of a pulse cycle.

slant arrow #3 for plots No. 1 to 8 in Fig. 5C). These phenomena indicate that the recirculation oscillates with time and space. As expected, the distal branch wall adjacent to the distal branch apex shows high positive shear rates. A shear rate of 1240 s^{-1} is observed at 0.11 s (i.e., arrow #1 plot No. 1 in Fig. 5D) during systole. The high shear rate is localized in nature and is reduced in magnitude as the fluid reaches downstream locations in the branch.

The wall shear stress which shows a combined effect of the non-Newtonian viscosity and shear rate is presented in Figs. 6A-6D along the wall of the main lumen and branch at various times 1-8 during the pulse cycle. At the downstream locations of both main and branch lumens the shear stress variation are oscillatory (i.e., arrow #2 in Fig. 6A) in nature, due to the tri-phasic nature of the pulse, having values in the range of 16 dynes/cm^2 to -12 dynes/cm^2. The oscillatory shear stress values vary as the fluid encounters the branch. At t = 0.16 sec, i.e., during the decelerating phase of systole, a combination of negative and positive shear stress is observed (i.e., arrow #1 for plot No. 3 in Fig. 6A), indicating the existence of a recirculating region at that instant of time. At the top wall near the proximal branch orifice, the shear stress reaches a value of 48 dynes/cm^2 at t = 0.16 s (i.e., arrow #1 for plot No. 2 in Fig. 6B) whereas it reaches -6.7 dynes/cm^2 at t = 0.202 sec, showing a sharp decrease in magnitude and a shift in positive direction of oscillatory shear stress. Similarly, at the top wall near the distal branch orifice, the shear rate reaches a value of 28 dynes/cm^2 at t = 0.16 (i.e., arrow #2 for plot No. 2 in Fig. 6B) whereas it reaches -(:s/cm^2 at t = 0.244 s. The shear stress at the proximal branch wall near the entry region of the branch shows a value of -33.6 dynes/cm^2 at t = 0.244 s (i.e., arrow #1 for plot No. 5 in Fig. 6C) indicating a shift in oscillatory shear to the negative direction, whereas the distal wall shows a value of 45.5 dynes/cm^2 (i.e., arrow #1 for plot No. 2 in Fig. 6D), a shift in oscillatory shear to the positive direction.

The variation of pulsatile pressure drop with time is presented in Figs. 7A-7D. The reference instantaneous pressure is considered at wall location of 1-s. Each plot represents pressure drop at different axial locations. Discrete bilinear pressure formulation is used to calculate the pressure data. The pulsed pressure drop is tri-phasic in nature due to the tri-phasic nature of the instantaneous velocity curve. Pressure changes include initial pressure drop and subsequent rise, followed by a drop. The maximum pressure drop of -0.9 mm Hg occurs at t = 0.055 s whereas the maximum pressure rise of 1.2 mm Hg occurs at 0.236 s. As compared to the times at which peak values of instantaneous input velocities and peak pressure drops occurs, a phase lag between the two peak values is observed. For accelerating flow during systole the pressure drop increases with time from t = 0.0 s to t = 0.055 s. In contrast, for decelerating flow of systole and accelerating negative flow of diastole, the pressure rises with time, till t = 0.236 s. As the flow accelerates in mid-diastole, Δp again drops to a near zero value at t = 0.332 s. The branch flow aids to increase the local pressure rise in the main lumen (i.e., shown by + sign in Figs. 7A and 7B) which, in other words, indicates a larger adverse pressure gradient. From the pressure drop data one can identify the adverse pressure gradient. Since it is difficult to isolate the flow separation regions, detail knowledge of velocity, shear rate and shear stress are required as described herein.

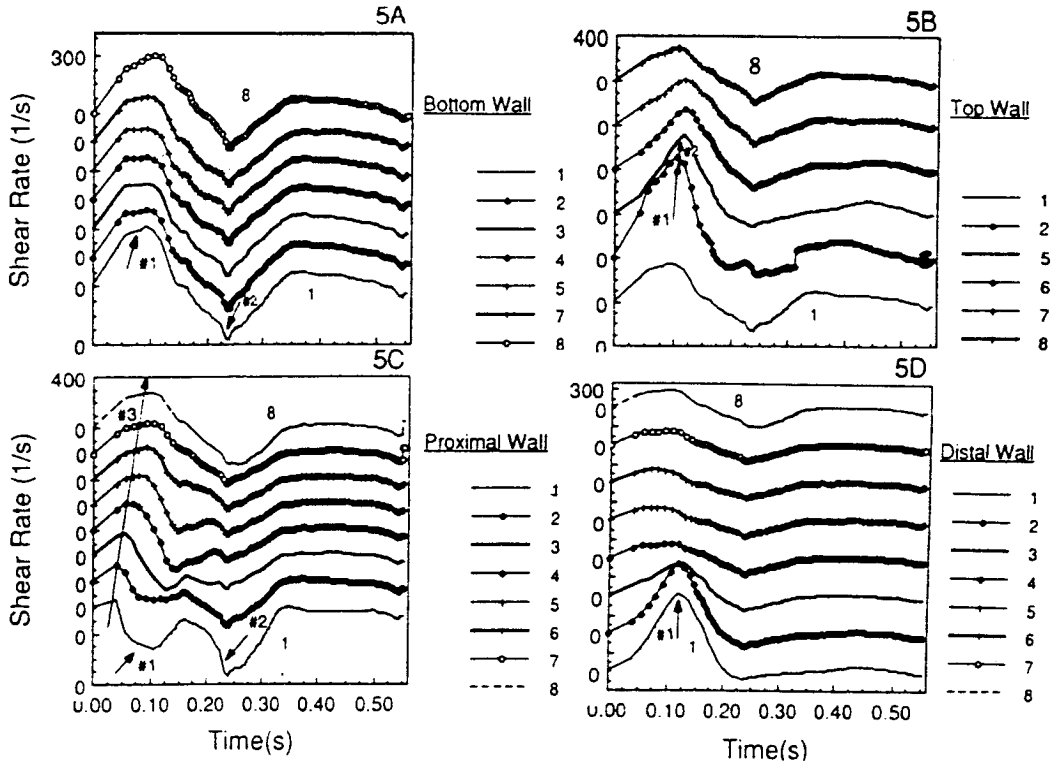

Fig. 5 Time histories of wall shear rate distributions of a pulse cycle in the main and branch lumen at various axial wall locations.

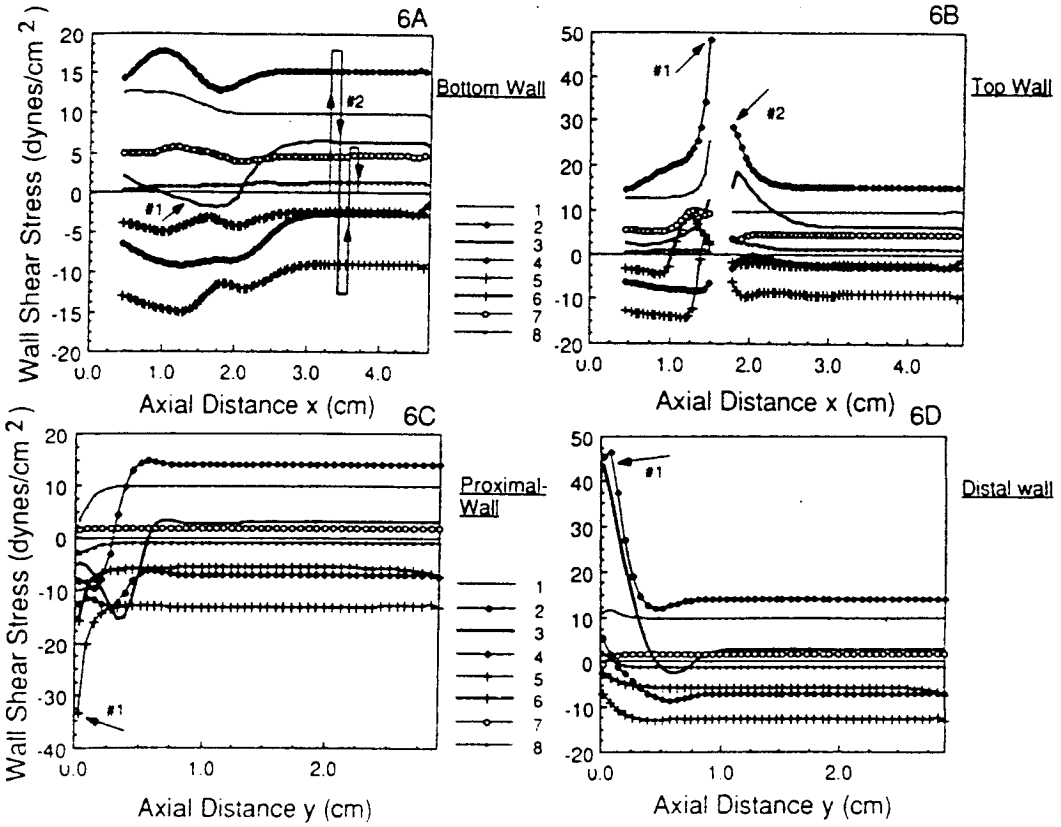

Fig. 6 Wall shear stress distribution along the wall of the main and branch lumen for different time steps of a pulse cycle.

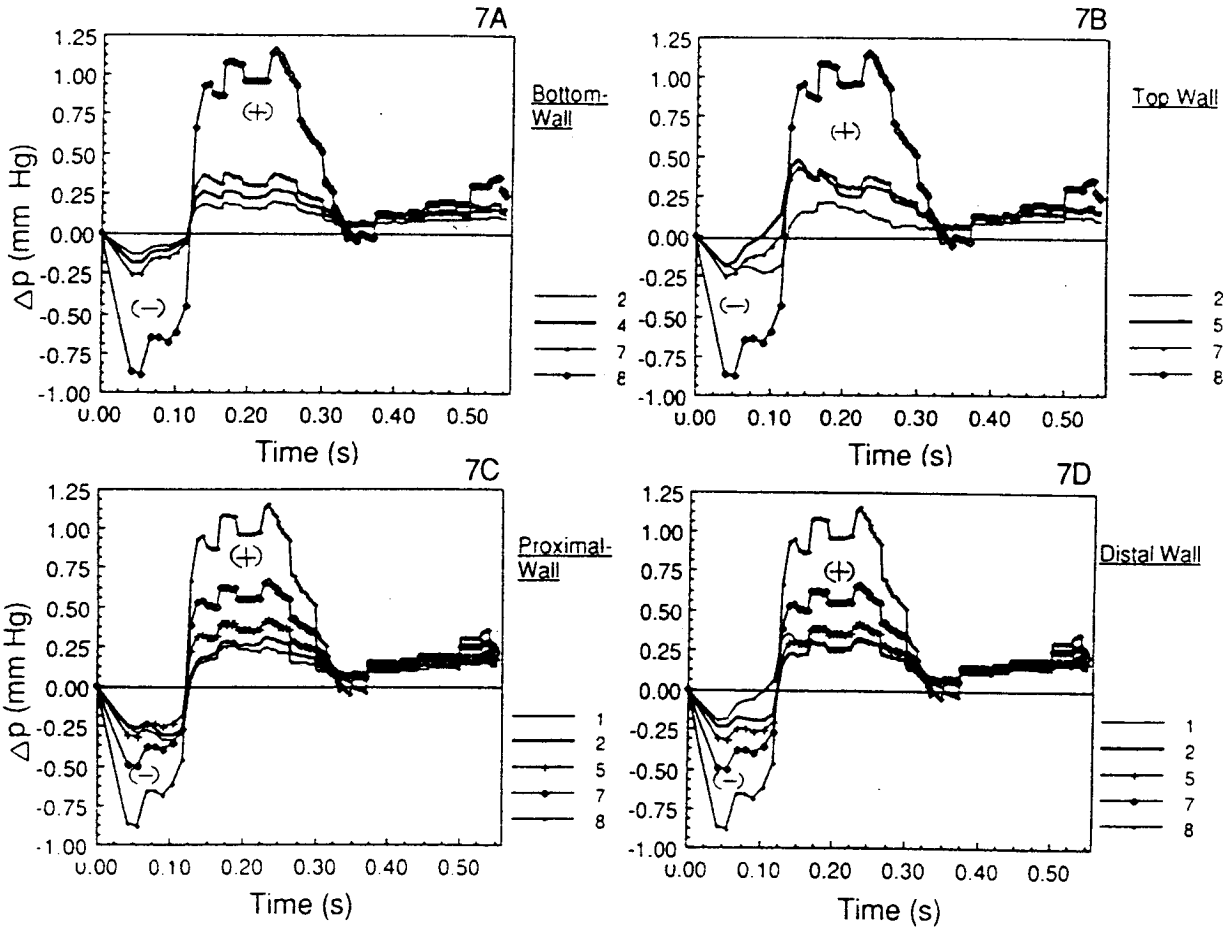

Fig. 7 Time histories of pressure drop distributions for a pulse cycle in the main and branch lumen at various axial wall locations.

SUMMARY AND CONCLUSION

The interesting observations are summarized as follows:

i) For a cardiac cycle, during systole, there are formation of two dominant recirculating zones e.g., one generated at the proximal wall of the branch lumen, and the other at the main lumen wall opposite to the branch. Further, due to the tri-phasic nature of the pulse, two additional recirculating zones are generated at the proximal wall and the wall opposite to the branch during mid-diastole. In comparison to mid-diastole, the recirculating zones during systole have a higher intensity, length and width. Also at the top wall, near the branch apex, mild recirculation zones are observed.

ii) The recirculating zones at branch locations not only oscillate with time but also move back and forth along the axial directions. In addition, recirculation height changes along the branch. Hence, the recirculating zones are functions of both temporal and spatial parameters.

iii) The changes in magnitude and direction of oscillatory wall shear stress values, adjacent to the entry region of branch lumen, are significantly higher than the straight lumen of the artery. Near the entry region of the branch, the distal wall shows higher shear stress with a value of 48 dynes/cm^2 as compared to a lower shear stress of -33 dynes/cm^2 at the proximal wall. The main lumen wall ...e proximal branch apex shows an oscillatory shear stress within the range of 48 dynes/cm^2 to -6.7 dynes/cm^2 which indicates a shift in positive direction as compared to the normal oscillatory wall shear stress. Also the main lumen wall near the distal branch apex shows a similar shift in the oscillatory shear stress within the range of 28 dynes/cm^2 to -6.2 dynes/cm^2. The main lumen wall, opposite to the branch, shows a larger range of oscillatory wall shear stress.

vi) The pressure drop becomes tri-phasic in nature due to the tri-phasic nature of the input velocity curve. Pressure changes include an initial pressure drop and subsequent pressure rise, followed by another pressure drop. The branch wall region contributes to the rise in the local pressure which indicates a larger adverse pressure gradient.

v) Repeated generation and shedding of recirculating vortices near the branch results in formation of time and space dependent changes in oscillatory wall shear stress and shear rate. Sharp changes in the magnitude and shift in oscillatory wall shear stress values, as compared to unbranched regions, may create unfavorable physiological conditions which may lead to increased intimal wall thickening and eventual development of lesions. The adverse physiological conditions are e.g., lipid deposition and depletion of oxygen transport due to lower level of oscillatory wall shear stress, whereas potential trauma to endothelial cells along arterial walls due to higher level of oscillatory wall shear stress, which, in combination, may be responsible for initiation and progression of plaques in branch regions.

REFERENCES

Back, L. H., Cho, Y. I. and Crawford, D. W. (1986) Phasic and spatial pressure measurements in a femoral artery branch model for pulsatile flow, *ASME Trans., Journal of Biomechanical Engineering*, **108**, 251-258.

Baker, A.J. (1983) *Finite Element Computational Fluid Mechanics*, Hemisphere Publishing Corp.

Banerjee, R.K., Cho, Y.I. and Back, L. H. (1992) Numerical studies of 3-D arterial flows in reverse curve geometry: Part I, Peak Flow, *ASME Trans., Journal of Biomechanical Engineering*, , [in press].

Banerjee, R.K., Cho, Y.I. and Back, L. H. (1992) Pressure drop in a tapered femoral artery of a dog: Pulsatile Flow, *Advances in Bioengineering, ASME*., **22**, 285-288.

Cho, Y. I., Back, L. H., and Crawford, D. W. (1985) Experimental investigation of branch flow ratio, angle, and Reynolds number effects on the pressure and flow fields in arterial branch models. *ASME J. Biomech. Engrg.*, **107**, 257-267.

Cho, Y.I. and Kensey, K.R. (1991) Effects of the non-Newtonian viscosity of blood on flows in a diseased arterial vessel: Part 1, Steady flows, *Biorheology*, **28**, 241-262.

Dewey, C. F. (1978) Fluid mechanics of arterial flow, *Advances in Experimental Medicine and Biology*, **115** (S. Wolf and N. T. Werthessen, Ed.), Chap. 2, 55-103.

FIDAP Manual, (1991), Fluid Dynamics International, Inc., Evanston, Illinois.

Fry, D. L. (1973) Responses of the arterial wall to certain physical factors, atherogenesis: Initiating factors, ed. R. Porter and J. Knight, Ciba Found. Symp. 12, *Elsevier*, 93-125.

Khodadadi, J. M. (1992) Wall pressure and shear stress variations in a 90-Deg Bifurcation during pulsatile laminar flow, ASME *Journal of Fluids Engineering*, **113**, 111-115.

Lutz, R. J. Hsu, L., Menawat, A., Zrubek, J., and Edwards K. (1983) Comparison of steady and pulsatile flow in a double branching arterial model. *Journal of Biomechanics*, **16**, 753-766.

Liepsch, D. and Moravec, S., Rastogi, A. K. and Vlachos, N. S. (1982) Measurements and calculations of laminar flow in a ninety degree bifurcation, *Journal of Biomechanics*, **15**, 473-485.

Moravec, S. and Liepsch, D. (1983). Flow investigation in a model of a three dimensional human artery with Newtonian and non-Newtonian Fluids (Part 1), *Biorheology*, **20**, 745.

Nerem, R. M. and Levesque, M. J. (1987) Fluid mechanics in atherosclerosis. *Handbook of Bioengineering* (R. Skalak and S. Chien Ed.) Chap. **21**, 21.1- 21.22.

Perktold, K. (1989) Non-Newtonian blood flow simulation and wall shear stress in an arterial bifurcation, *Proc. 2nd Int. Symp. on Bioflud Mechanics & Biorheology*, 685-694, Munich, W. Germany.

Risoe, C. and Wille, S. O. (1978) Blood velocity in human arteries measured by a bidirectional ultrasound doppler flowmeter, *Acta Physiol. Scand.*, **103**, 370-378.

Schultz, D. L. (1972) Pressure and flow in large arteries. *Cardiovascular Fluid Dynamics* **1**, (D. H. Bergel, Ed.), 287-314, Academic Press.